

Chapter 8: Climate Models and Their Evaluation

Coordinating Lead Authors: David Randall (USA), Richard A. Wood (UK)

Lead Authors: Sandrine Bony (France), Robert Colman (Australia), Thierry Fichefet (Belgium), John Fyfe (Canada), Vladimir Kattsov (Russia), Andrew Pitman (Australia), Jagadish Shukla (USA), Jayaraman Srinivasan (India), Ronald J. Stouffer (USA), Akimasa Sumi (Japan), Karl Taylor (USA)

Contributing Authors: K. Achuta Rao (USA), R. Allan (UK), A. Berger (Belgium), H. Blatter, C. Bonfils (USA), A. Boone (France), C. Bretherton (USA), T. Broccoli (USA), V. Brovkin (Germany), W. Cai (Australia), M. Claussen (Germany), P. Dirmeyer (USA), C. Doutriaux (USA), H. Drange (Norway), J.-L. Dufresne (France), S. Emori (Japan), A. Frei (USA), A. Ganopolski (Germany), P. Gent (USA), P. Gleckler (USA), H. Goosse (Belgium), R. Graham (UK), J. Gregory (UK), R. Gudgel (USA), A. Hall (USA), S. Hallegatte (France), H. Hasumi (Japan), A. Henderson-Sellers, H. Hendon (Australia), K. Hodges (UK), M. Holland (USA), A.A.M.. Holtslag (The Netherlands), E. Hunke (USA), P. Huybrechts (Belgium), W. Ingram (UK), F. Joos (Switzerland), B. Kirtman (USA), S. Klein (USA), R. Koster (USA), P. Kushner (Canada), J. Lanzante (USA), M. Latif (Germany), G. Lau (USA), M. Meinshausen (USA), A.H. Monahan (Canada), J. Murphy (UK), T. Osborn (UK), T. Pavlova (Russia), V. Petoukhov (Germany), T. Phillips (USA), S. Power (Australia), S. Rahmstorf (Germany), S. Raper (UK), H. Renssen (The Netherlands), D. Rind (USA), M. Roberts (UK), A. Rosati (USA), C. Schär (Switzerland), J. Scinnoca (Canada), A. Schmittner (USA), D. Seidov (USA), A.G. Slater (USA), D. Smith (UK), B. Soden (USA), W. Stern (USA), D. Stone (UK), K.Sudo (Japan), G. Tselioudis (USA), M. Webb (UK), M. Wild (Switzerland), T. Yakemura (Japan).

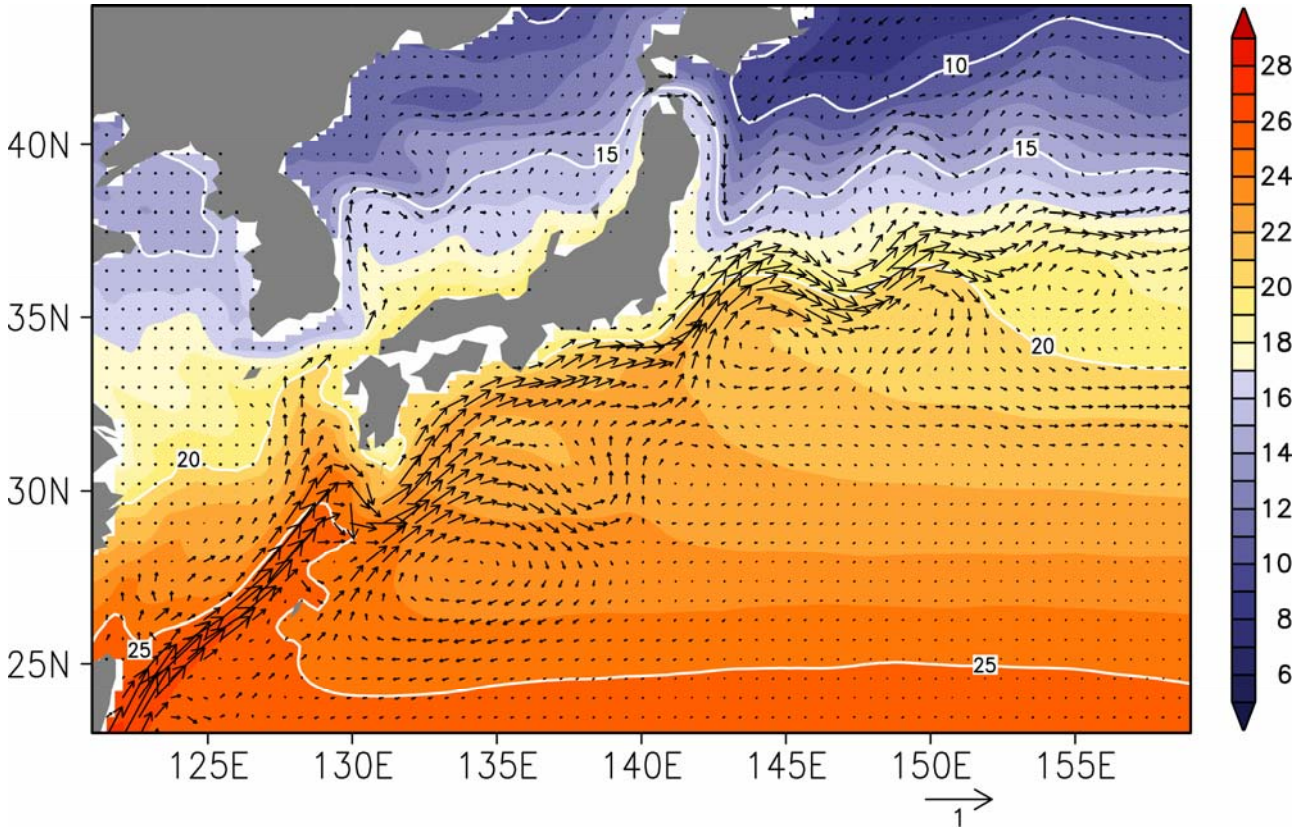
Review Editors: Elisa Manzini (Italy), Taroh Matsuno (Japan), Bryant McAvaney (Australia)

Date of Draft: 3 March 2006

Notes: TSU compiled version

1 **Figures**

2

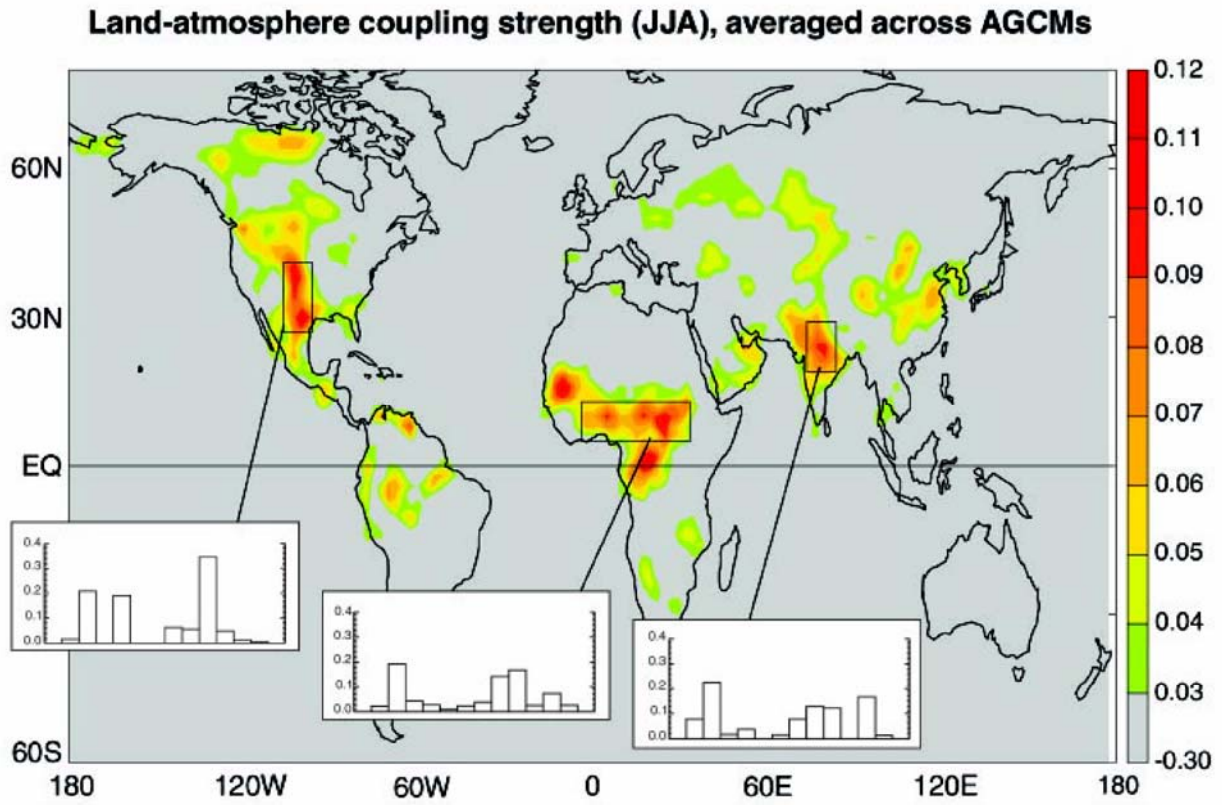


3

4

5 **Figure 8.2.1.** Long-term mean ocean current velocities at 100m depth (vectors, unit: $m s^{-1}$) and sea surface
 6 temperature (color shades, unit: $^{\circ}C$) around the Kuroshio and the Kuroshio Extension obtained from a
 7 control experiment which is forced by pre-industrial conditions (CO_2 concentration 295.9 ppm) using
 8 MIROC3.2_hires.
 9

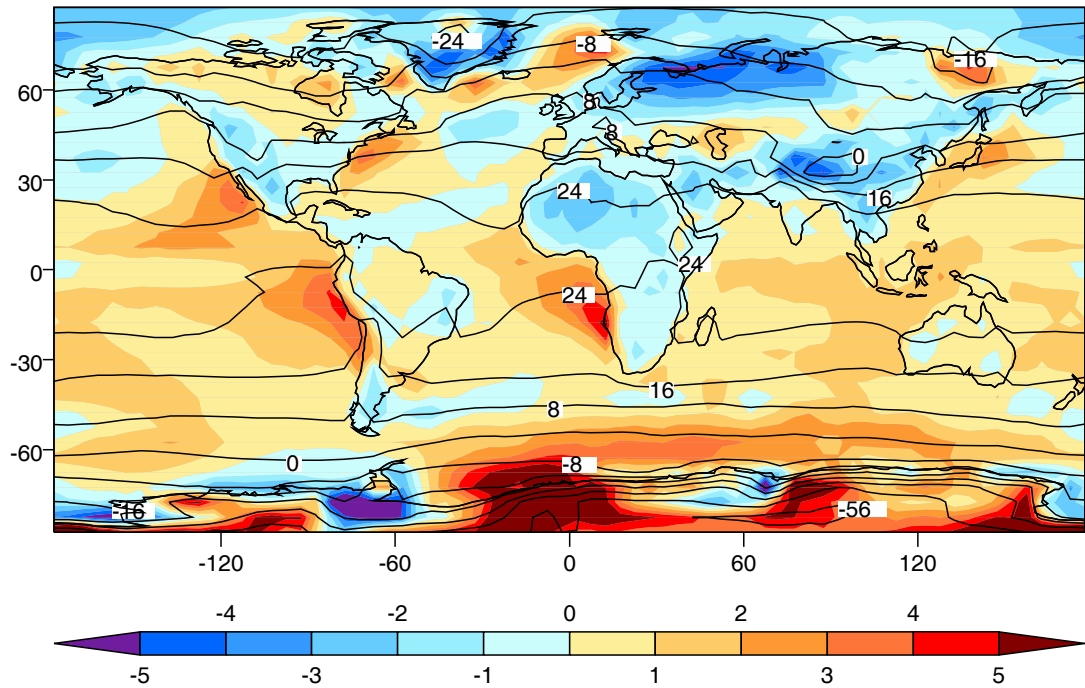
1
2



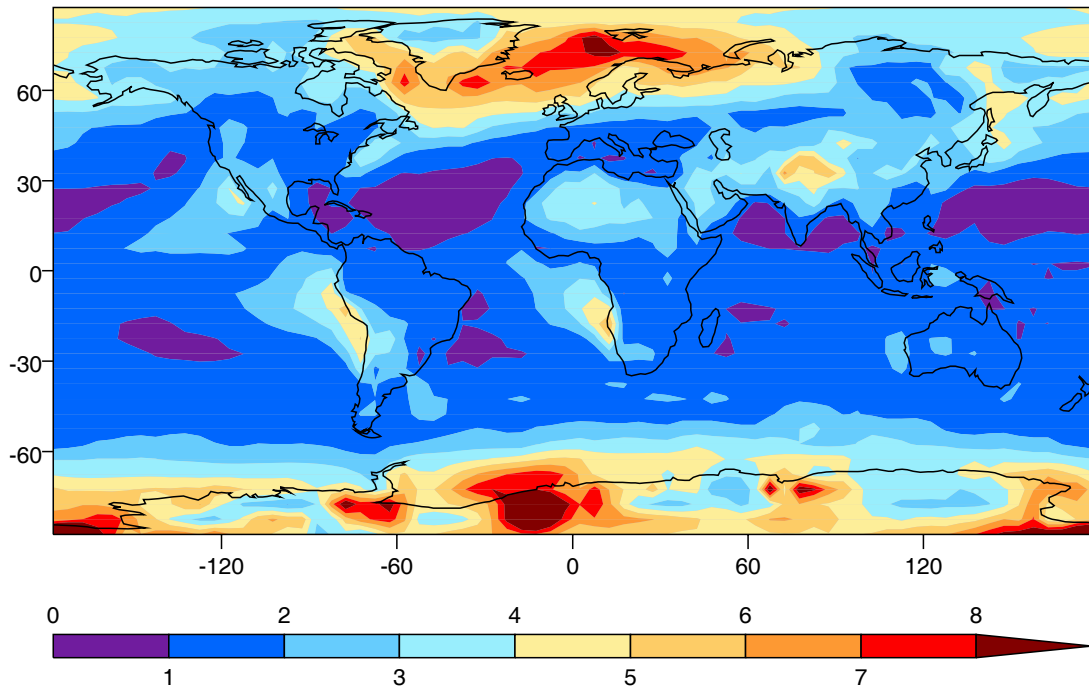
3
4
5
6
7
8
9
10

Figure 8.2.2. The land-atmosphere coupling strength diagnostic for boreal summer (the difference, dimensionless, describing the impact of soil moisture on precipitation), averaged across the 12 models participating in GLACE. **(Insets)** Areal averaged coupling strengths for the 12 individual models over the outlined, representative hotspot regions. No signal appears in southern South America or at the southern tip of Africa.

1 a)
2



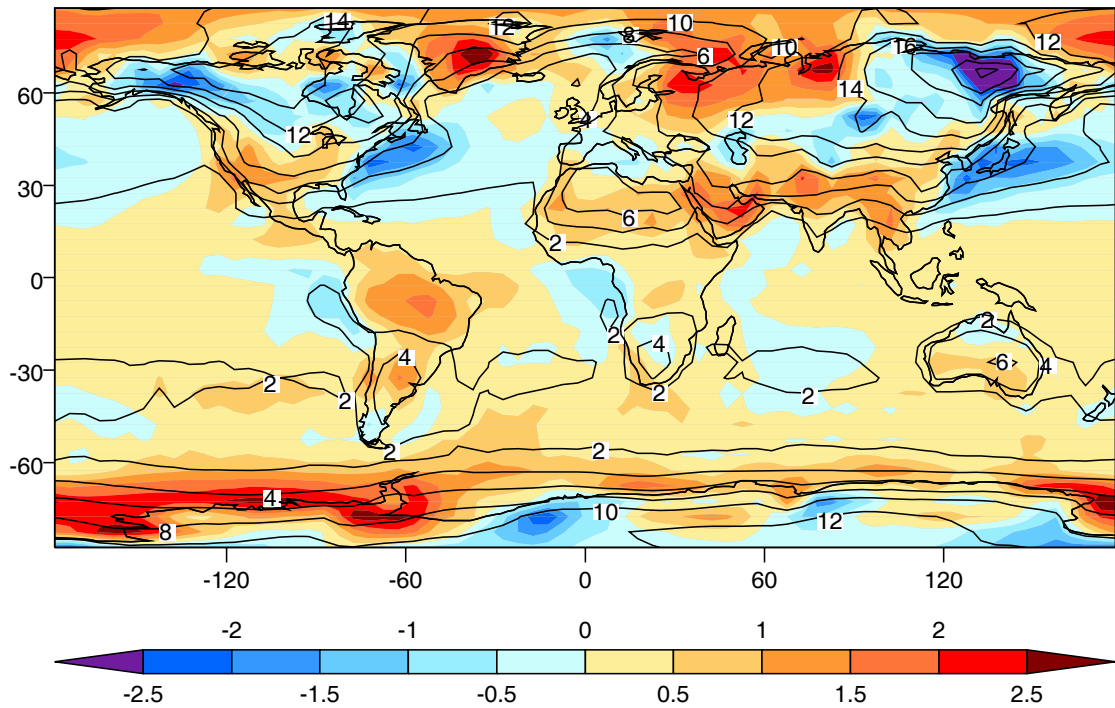
3 b)
4
5



6
7
8
9
10
11
12
13
14
15

Figure 8.3.1. Observed climatological annual-mean sea surface temperature (SST) and, over land, surface air temperature (labeled contours in panel a) and the multi-model mean error in these temperatures, simulated minus observed (color-shaded contours in panel a); also typical model error, as gauged by the root-mean-square model error in this temperature, based on all available IPCC model simulations (panel b). The observations are from the CRU merged SST and surface air temperature dataset for the period 1961–1990 (Jones et al., 1999), and the model results are from years 1980–1999 of the CMIP 20th Century simulations. Temperature units are °C.

1
2

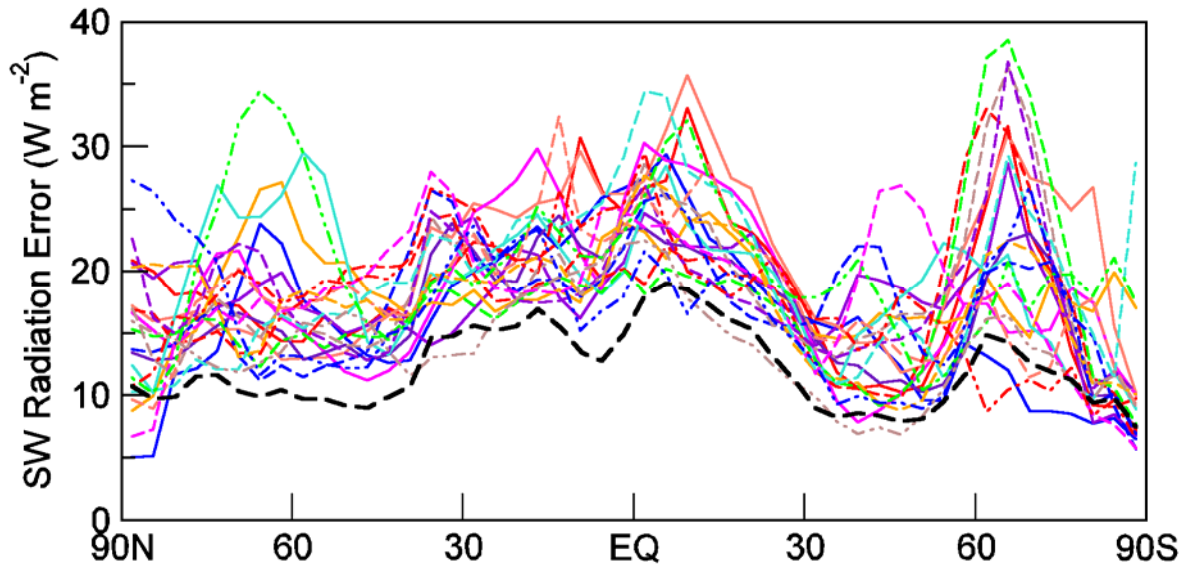


3
4
5
6
7
8
9
10
11
12

Figure 8.3.2. Observed standard deviation (labeled contours) of sea surface temperature (SST) and, over land, surface air temperature, computed over the climatological monthly mean annual cycle, and the multi-model mean error in the standard deviations, simulated minus observed (color-shaded contours). In most regions, the standard deviation provides a measure of the amplitude of the seasonal range of temperature. The observations are from the CRU merged SST and surface air temperature dataset for the period 1961–1990 (Jones et al., 1999), and the model results are from years 1980–1999 of the CMIP 20th Century simulations. Temperature units °C.

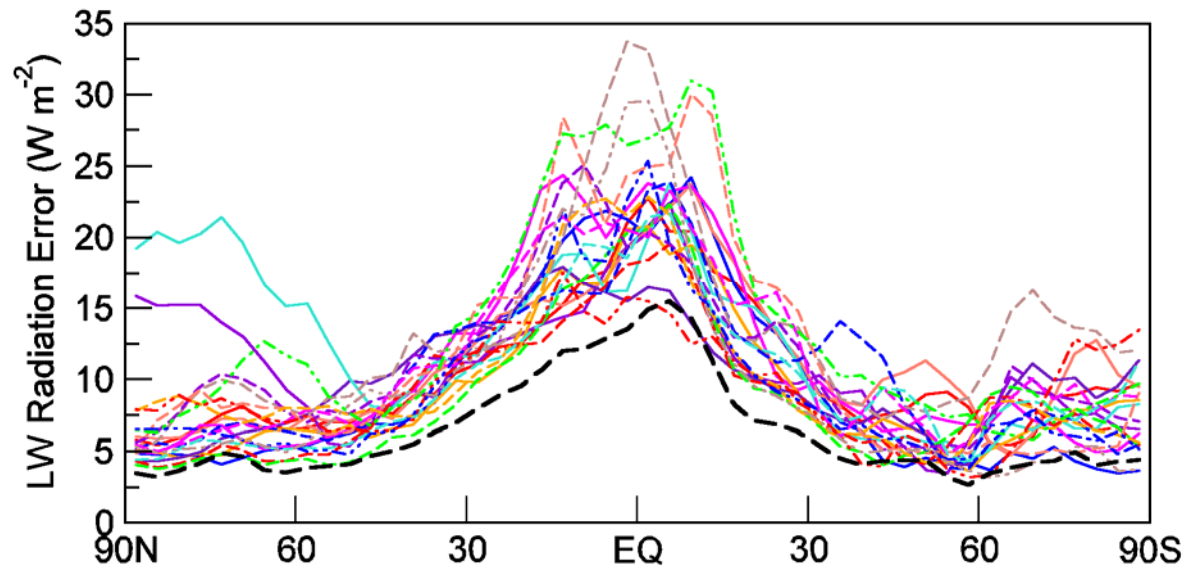
1

a)



2
3

b)

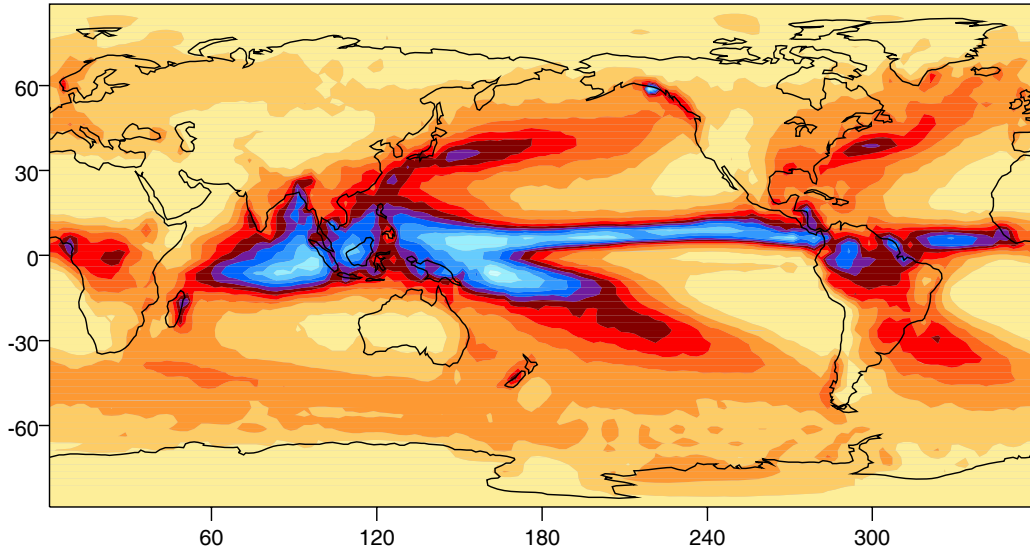


- | | | |
|-----------------|---------------|--------------------|
| — BCC-CM1 | — ECHO-G | — IPSL-CM4 |
| — BCCR-BCM2.0 | — FGOALS-g1.0 | — MIROC3.2(hires) |
| — CCSM3 | — GFDL-CM2.0 | — MIROC3.2(medres) |
| — CGCM3.1(T47) | — GFDL-CM2.1 | — MRI-CGCM2.3.2 |
| — CGCM3.1(T63) | — GISS-AOM | — PCM |
| — CNRM-CM3 | — GISS-EH | — UKMO-HadCM3 |
| — CSIRO-Mk3.0 | — GISS-ER | — UKMO-HadGEM1 |
| — ECHAM5/MPI-OM | — INM-CM3.0 | — Mean Model |

4
5
6
7
8
9
10
11
12
13

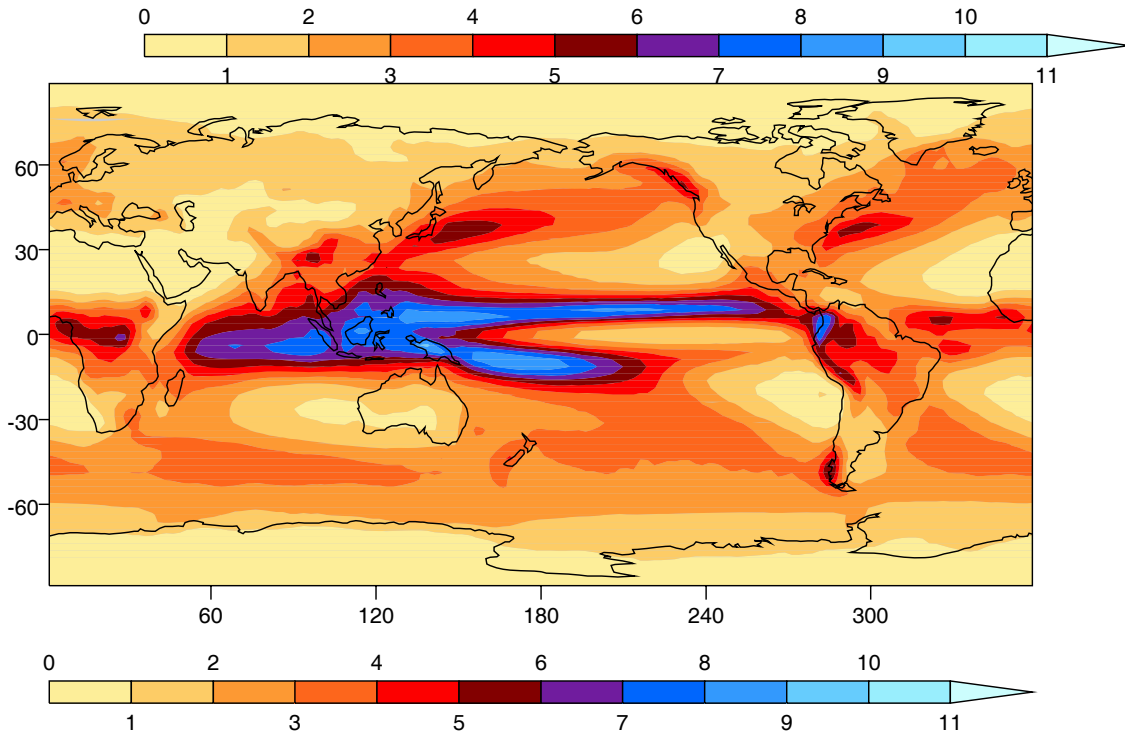
Figure 8.3.3. Root-mean-square (RMS) model error, as a function of latitude, in simulation of outgoing shortwave radiation scattered and reflected to space (panel a) and outgoing longwave radiation (panel b). The RMS error is calculated over all longitudes and over all months. The mean model result is computed by first calculating the multi-model monthly mean fields, and then calculating the RMS error (i.e., it is not the mean of the individual model RMS errors). The observational estimates are from radiometers carried by satellites during the period 1985–1989 (ERBE, Barkstrom et al., 1989), and the model results are from years 1980–1999 of the CMIP 20th Century simulations.

1 a)



2
3
4

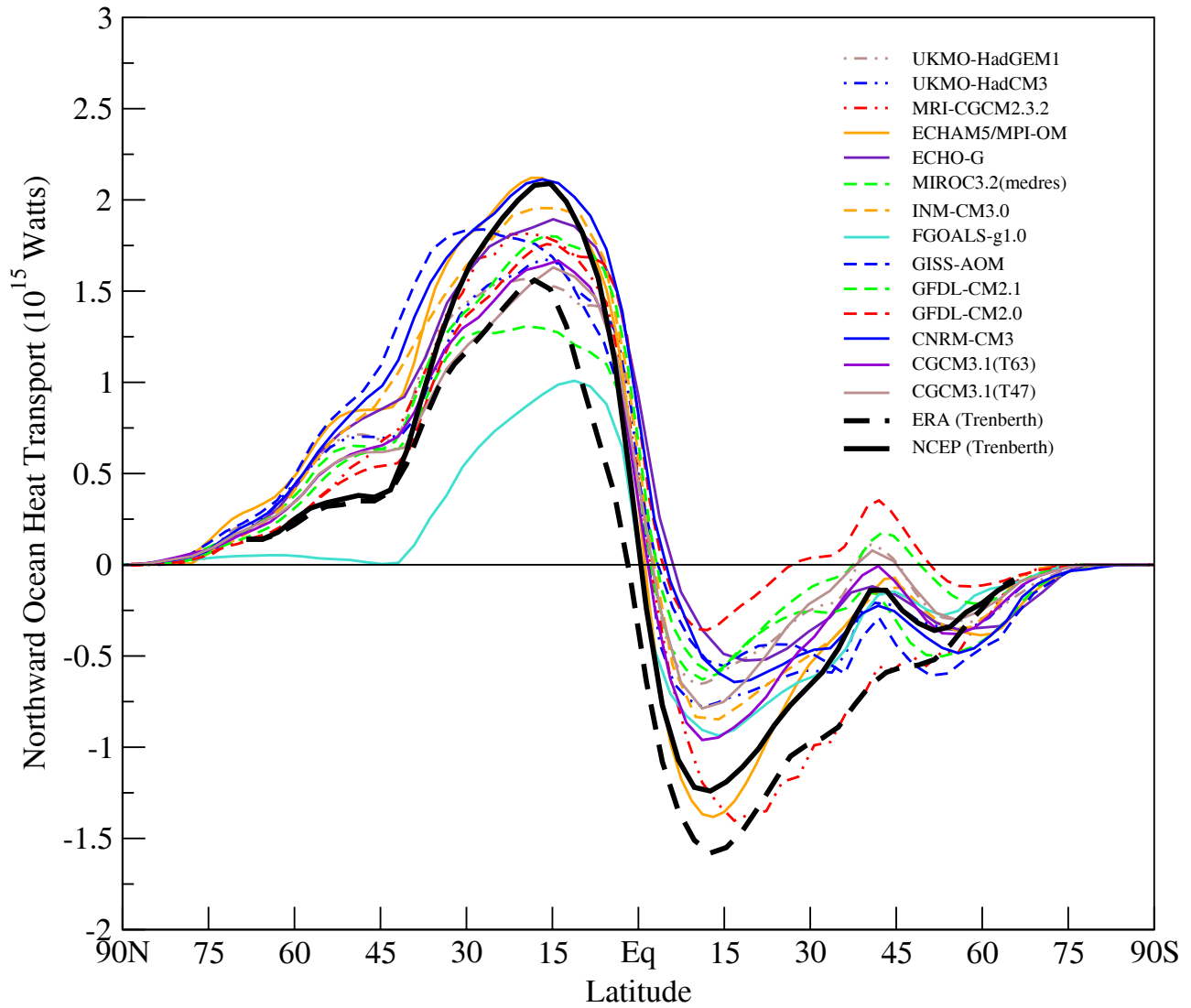
b)



5
6
7
8
9
10

Figure 8.3.4. Annual-mean precipitation rate (mm/day), observed (panel a) and simulated (panel b), based on the multi-model mean. The observational estimates are from Xie and Arkin (1997) for the period 1979–1993, and the model results are from years 1980–1999 of the CMIP 20th Century simulations.

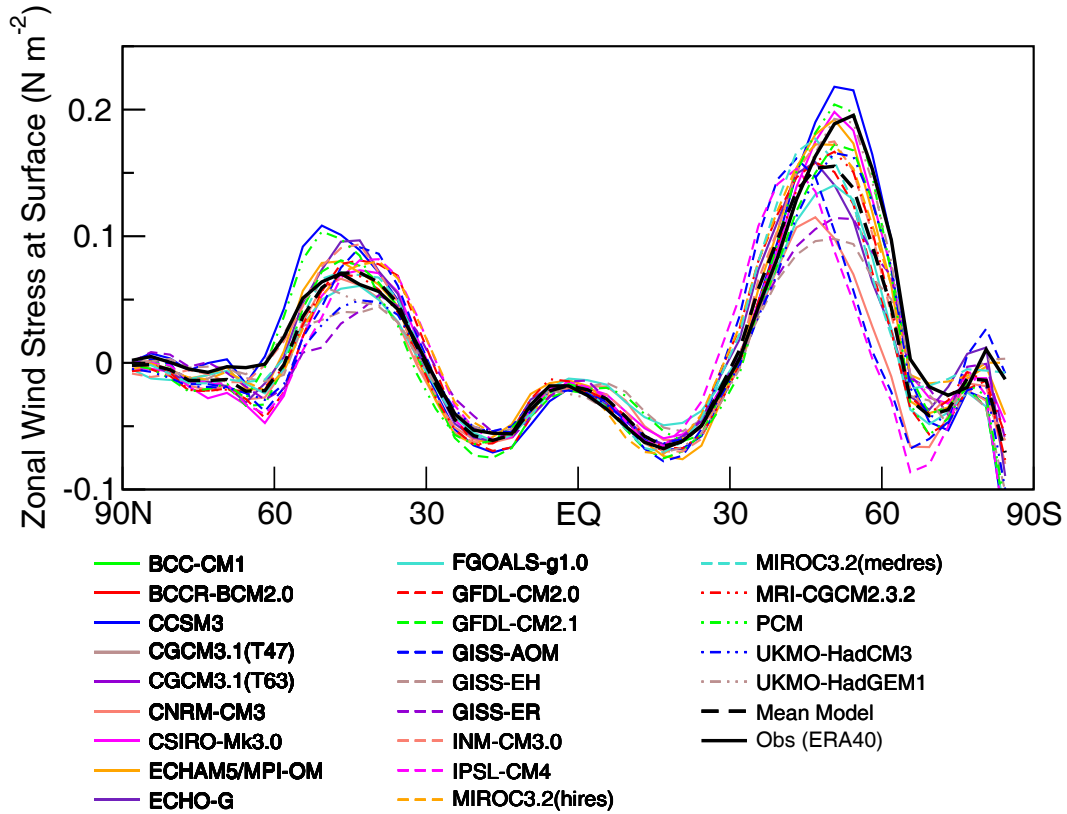
1
2



3
4
5
6
7
8
9

Figure 8.3.5. Annual mean, zonally averaged implied oceanic heat transport. The observationally-based estimates, taken from Trenberth and Caron (2001) for the period February 1985 to April 1989, are based on reanalysis products from NCEP/NCAR (Kalnay et al., 1996) and ERA40 (Uppala et al., 2005). The model results are from years 1980–1999 of the CMIP 20th Century simulations.

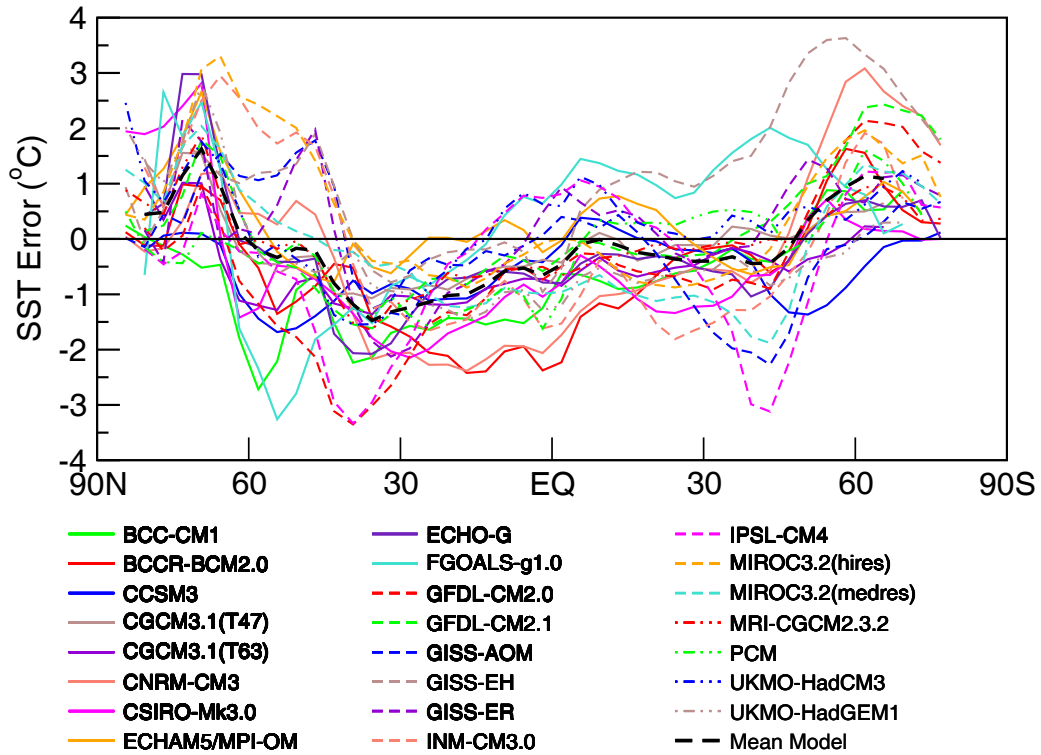
1
2



3
4
5
6
7
8
9

Figure 8.3.6. Surface zonal wind stress, annually and zonally averaged over the oceans. The observationally-based estimates are from the 40-year European Reanalysis for the period 1960–2000 (ERA40; Uppala et al., 2005), and the model results are from years 1980-1999 of climate of the CMIP 20th Century simulations.

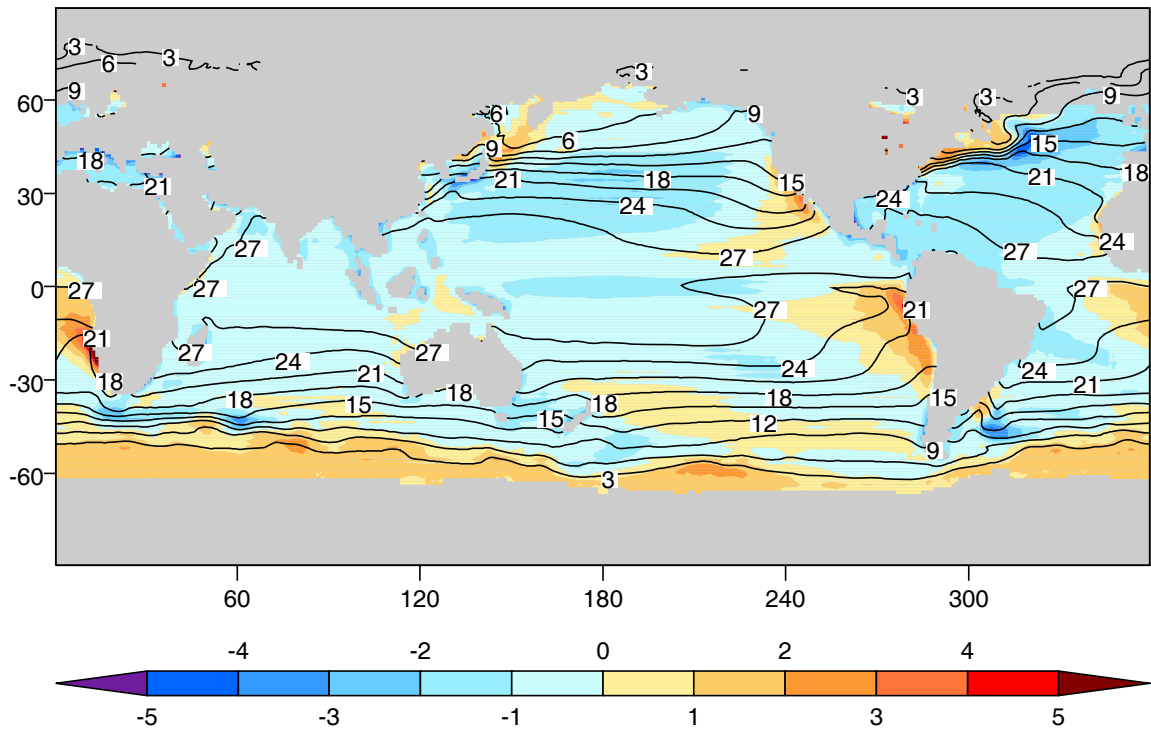
1
2



3
4
5
6
7
8

Figure 8.3.7. Zonally averaged, time mean sea surface temperature (SST) error, simulated minus observed. The observations are from years 1980–1999 of the HadISST data set (Rayner et al., 2003), and the model results are from years 1980–1999 of climate of the CMIP 20th Century simulations.

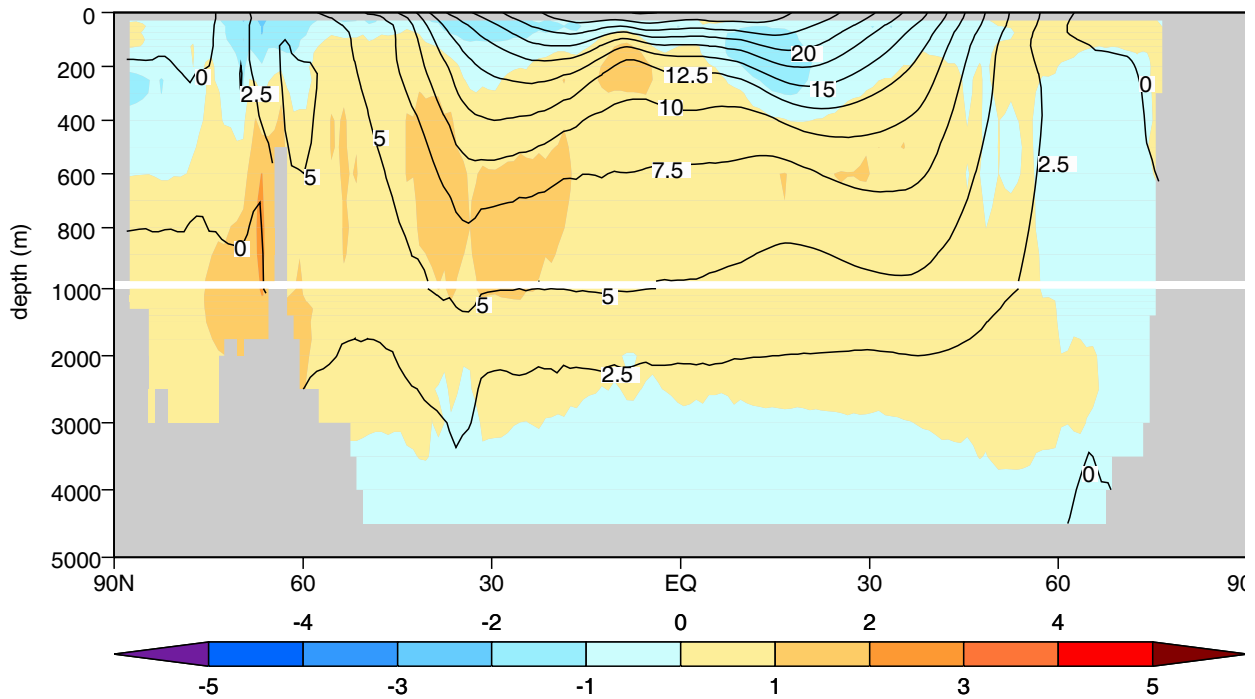
1
2



3
4
5
6
7
8
9
10

Figure 8.3.8. Observed sea surface temperature (labeled contours) and multi-model mean SST error, simulated minus observed (color-filled contours). Regions with sea ice have been masked because SST is unavailable from most models in these regions. The observations are from years 1961–1990 of the HadISST SST data set (Rayner et al., 2003), and the model results are from years 1980–1999 of the CMIP 20th Century simulations. Temperature units are °C.

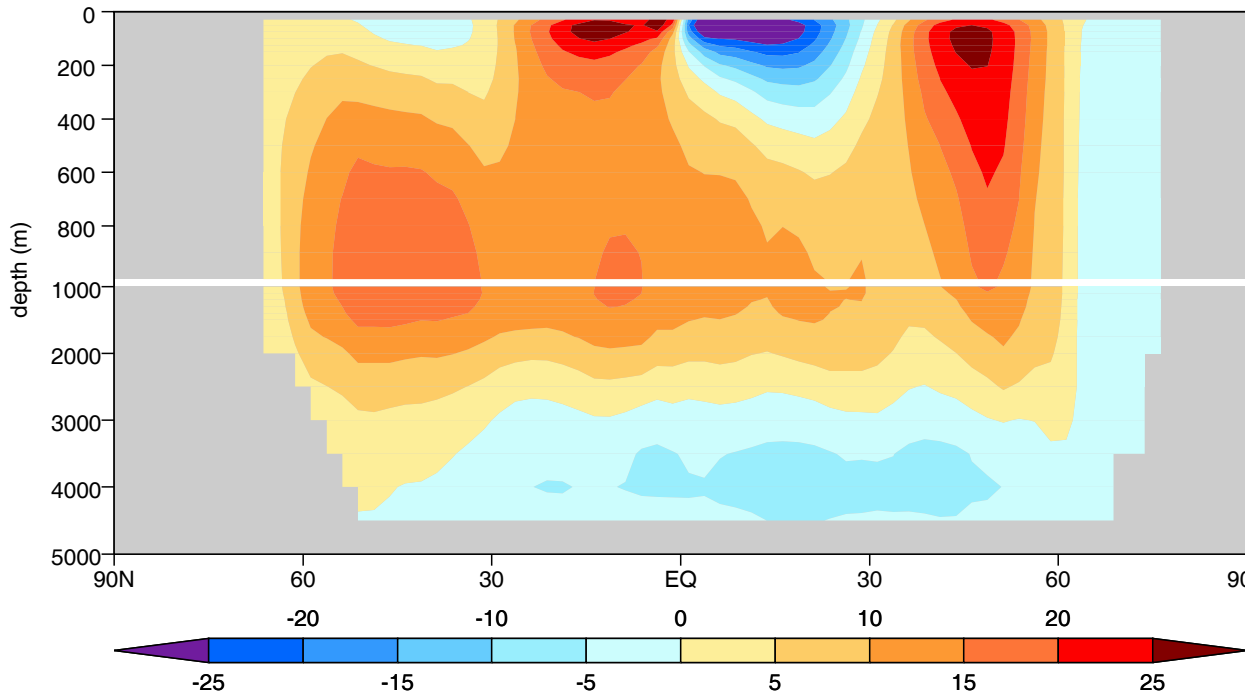
1
2



3
4
5
6
7
8
9
10

Figure 8.3.9. Observed climatological annual-mean potential temperature, zonally averaged over all ocean basins (labeled contours) and multi-model mean error in this field, simulated minus observed (color-filled contours). The observations are from the 2004 World Ocean Atlas (WOA-2004) compiled by Levitus, et al. (2005) for the period 1955–1998, and model results are from years 1950-1999 of the CMIP 20th Century simulations. Temperature units are °C.

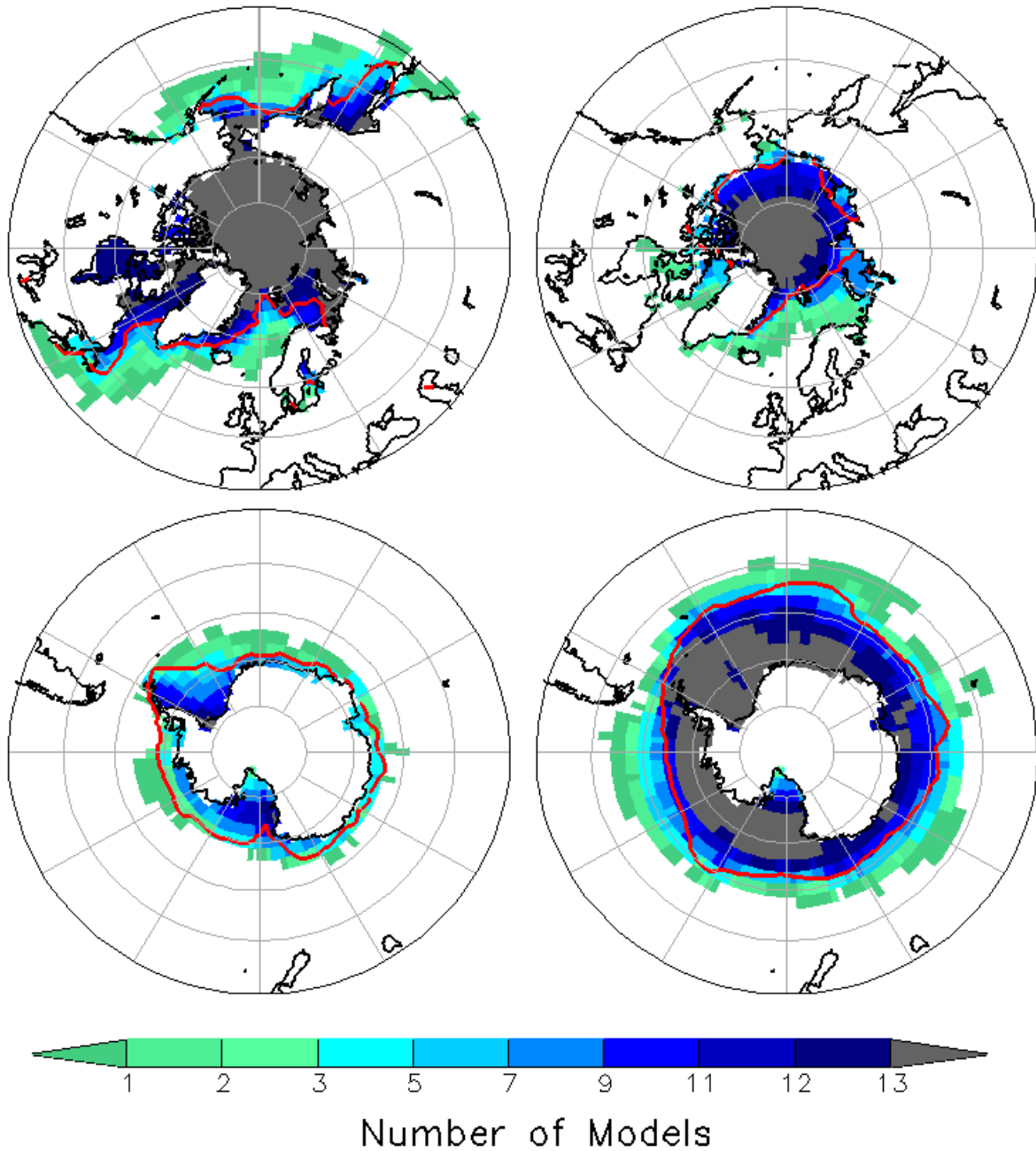
1
2



3
4
5
6
7
8

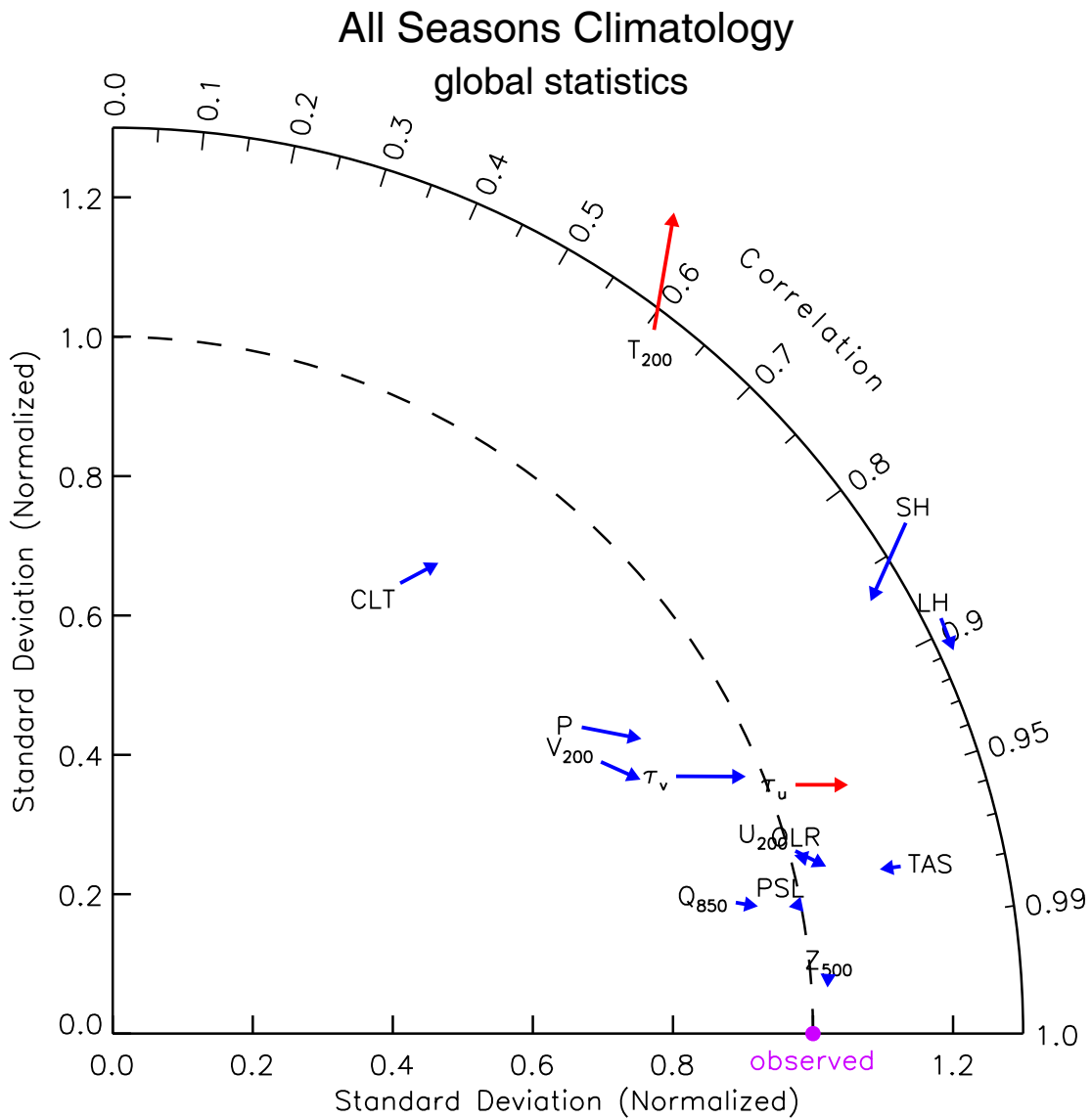
Figure 8.3.10. Zonally averaged meridional streamfunction computed across all basins (Sv). Positive values (brown colors) imply subsidence on the northern side, southward flow below, and ascending water to the south. The flow is in the opposite sense around negative values (blue colors).

1
2



3
4 **Figure 8.3.11.** Baseline climate (1980–1999) sea-ice distribution in the Northern Hemisphere (upper panels)
5 and Southern Hemisphere (lower panels) simulated by fourteen of the AOGCMs listed in Table 8.3.1 for
6 March (left) and September (right), adapted from Arzel et al. (2005). For each 2.5° x 2.5° longitude-latitude
7 grid cell, the figure indicates the number of models that have at least 15% of the area covered by sea ice. The
8 observed 15%-concentration boundaries (red line) are based on HadISST (Rayner et al., 2003).
9

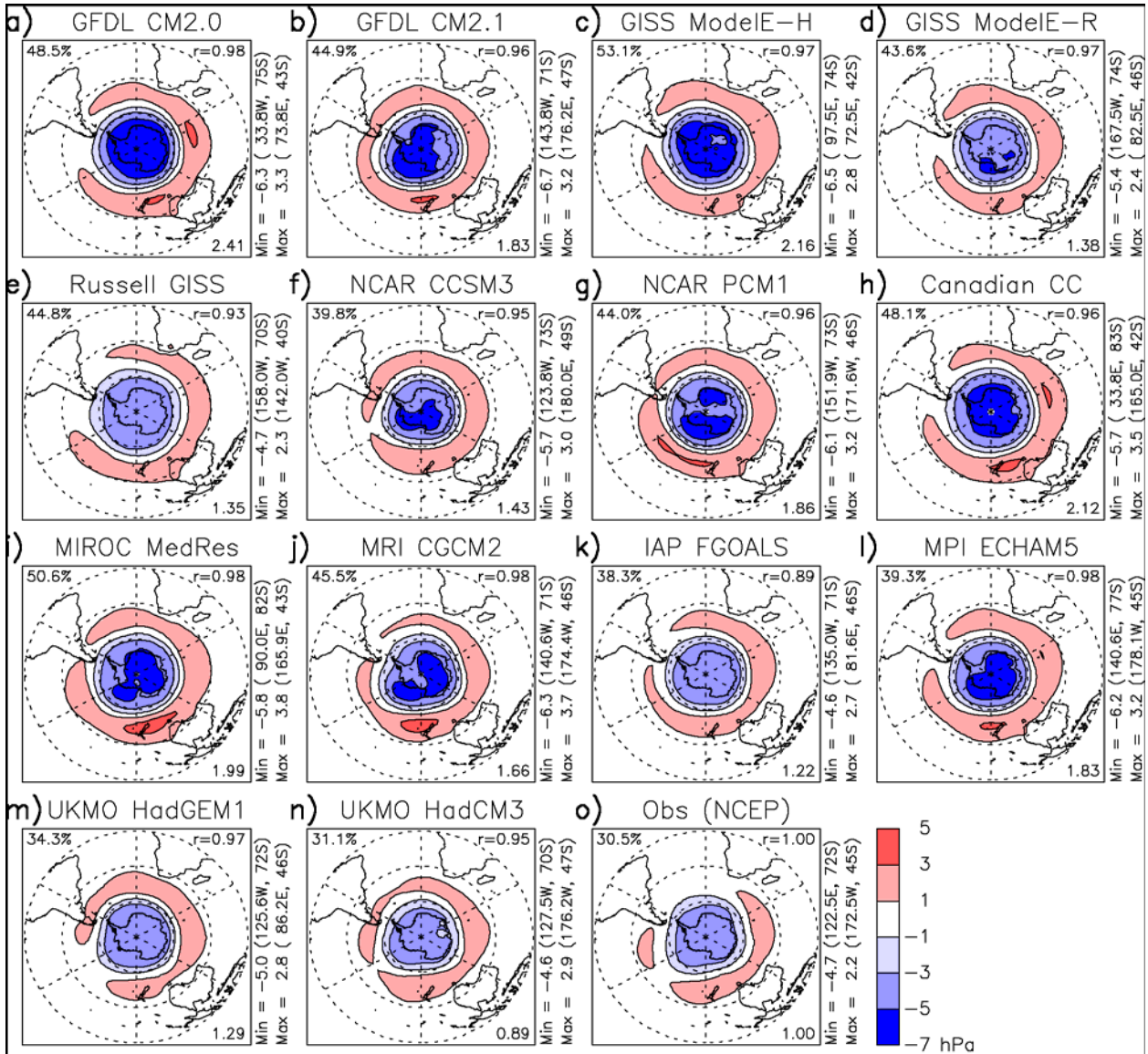
1
2



3
4
5
6
7
8
9
10
11
12
13
14
15
16
17
18
19
20
21

Figure 8.3.12. Changes in statistics characterizing AMIP model performance, based on the composite multi-model median fields (see text for further description). The fields analyzed were: surface air temperature (TAS) 500 hPa geopotential height (Z₅₀₀), 200 hPa zonal and meridional wind (U₂₀₀ and V₂₀₀), zonal and meridional components of surface wind stress over the oceans (τ_u and τ_v), mean sea level pressure over the oceans, (PSL), precipitation (P), cloud fraction (CLT), outgoing longwave radiation (OLR), 200 hPa temperature (T₂₀₀), 850 hPa specific humidity (Q₈₅₀), surface air temperature over land, and surface sensible and latent heat flux (SH and LH). Simulated fields were compared to ERA-15 (Gibson et al., 1997), with the following exceptions: P was compared to CPC (Xie and Arkin, 1997), CLT was compared to ISCCP (Schiffer and Rossow, 1985), OLR was compared to ERBE (Barkstrom et al., 1989), TAS was compared to CRU (Jones et al., 1999), and SH, LH, τ_u and τ_v were compared to the SOC Atlas climatology (Josey et al., 1998). The statistics shown on the diagram are the correlation coefficient between the observed and simulated field (related to the azimuthal angle), the root-mean-square (RMS) difference between the two fields (proportional to the distance to the point on the x-axis marked observed), and the standard deviation (SD) of the simulated field (proportional to the radial distance). The dimensional statistics (RMS error and SD) have been normalized by the observed SD, and the RMS error is computed after removal of generally negligible global mean biases.

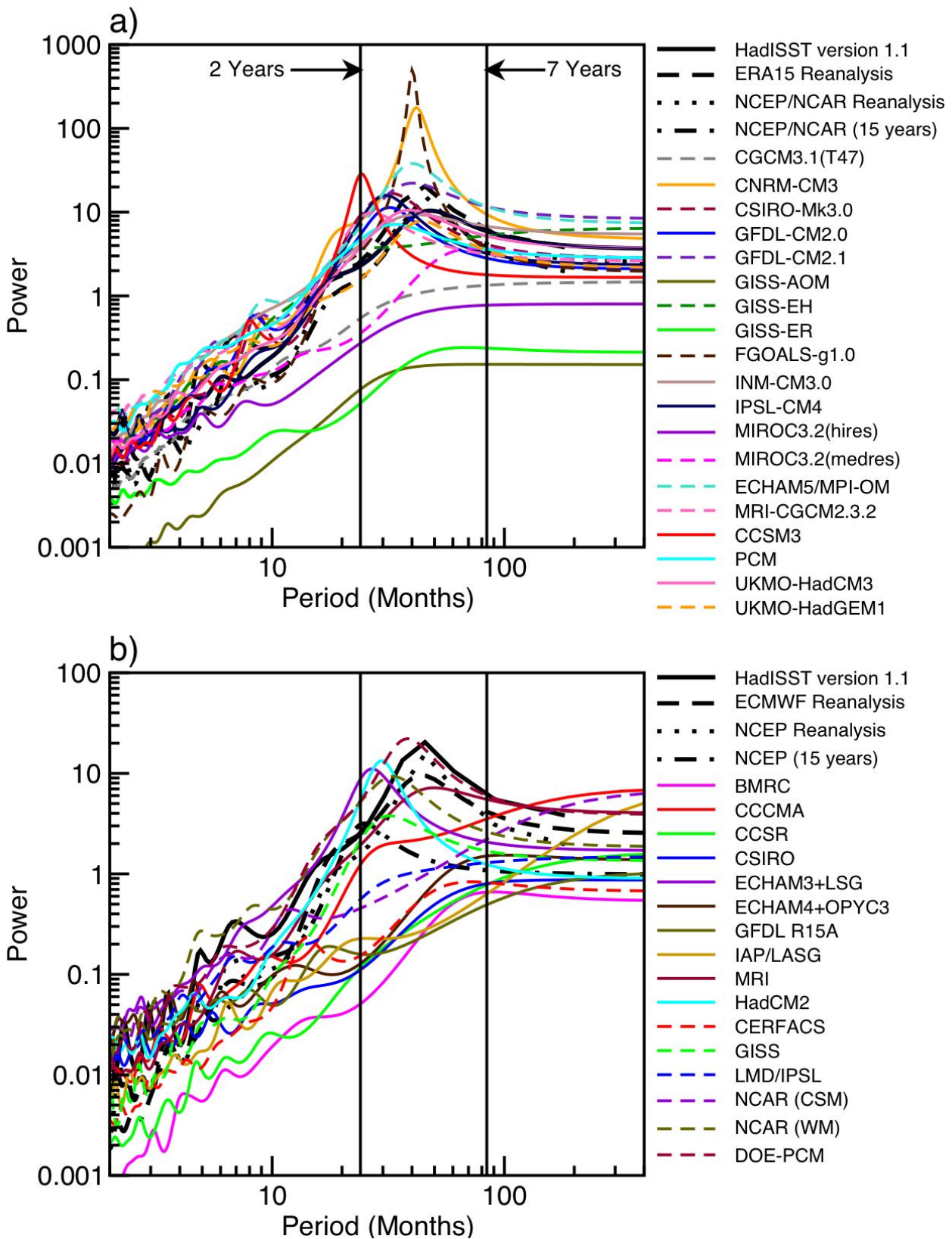
1
2



3
4
5
6
7
8
9
10

Figure 8.4.1. Ensemble mean leading EOF of summertime (November through February) SH SLP (hPa) for 1950–1999. The EOFs are scaled so that the associated PC has unit variance over this period. The percentage of variance accounted for by the leading mode is listed at the upper left corner of each panel. The spatial correlation (r) with the observed pattern is given at the upper right corner. At the lower right is the ratio of the EOF spatial variance of the observed value. Adapted from Miller et al. (2006).

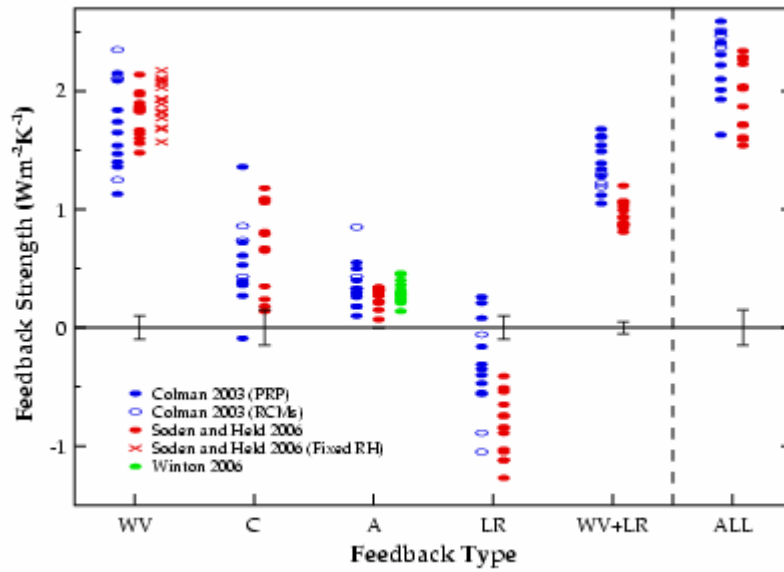
1
2



3
4
5
6
7
8
9

Figure 8.4.2. Maximum entropy power spectra of NINO3 (5°N–5°S, 150°W–90°W) surface air temperature for a) the IPCC models and b) the CMIP2 models (after Figure 4 in AchutaRao and Sperber, 2002). The vertical lines correspond to periods of 2 and 7 years. The power spectra from the reanalyses and for SST from the HadISST version 1.1 dataset are given by the series of solid, dashed, and dotted black curves. Adapted from AchutaRao and Sperber (2006).

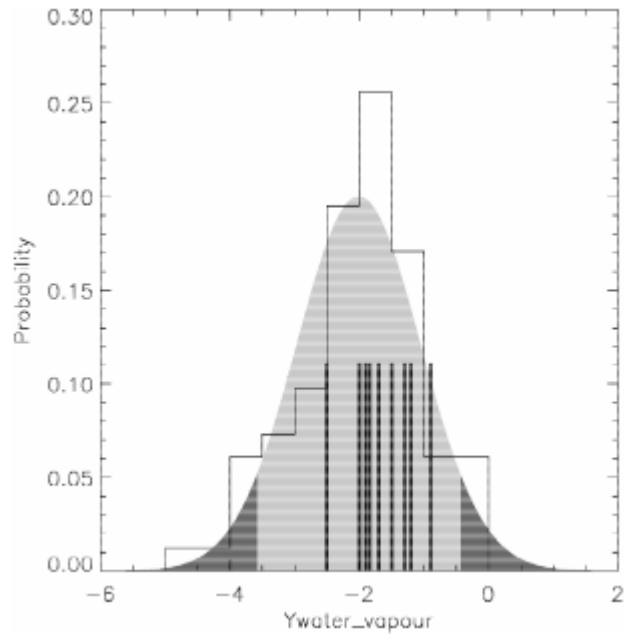
1
2



3
4
5
6
7
8
9
10
11
12
13
14

Figure 8.6.1. Comparison of GCM climate feedback parameters for water vapour (WV), cloud (C), surface albedo (A), lapse rate (LR) and the combined water vapour + lapse rate (WV+LR) in units of $W m^{-2} K^{-1}$. "ALL" represents the sum of all feedbacks. Results are taken from Colman (2003) (blue), Soden and Held (2006) (red) and Winton (2006a) (green). Closed and open symbols from Colman (2003) represent calculations determined using the partial radiative perturbation (PRP) and the radiative-convective method (RCM) approaches respectively. Crosses represent the water vapour feedback computed for each model from Soden and Held (2006) assuming no change in RH. Vertical bars depict the estimated uncertainty in the calculation of the feedbacks from Soden and Held (2006).

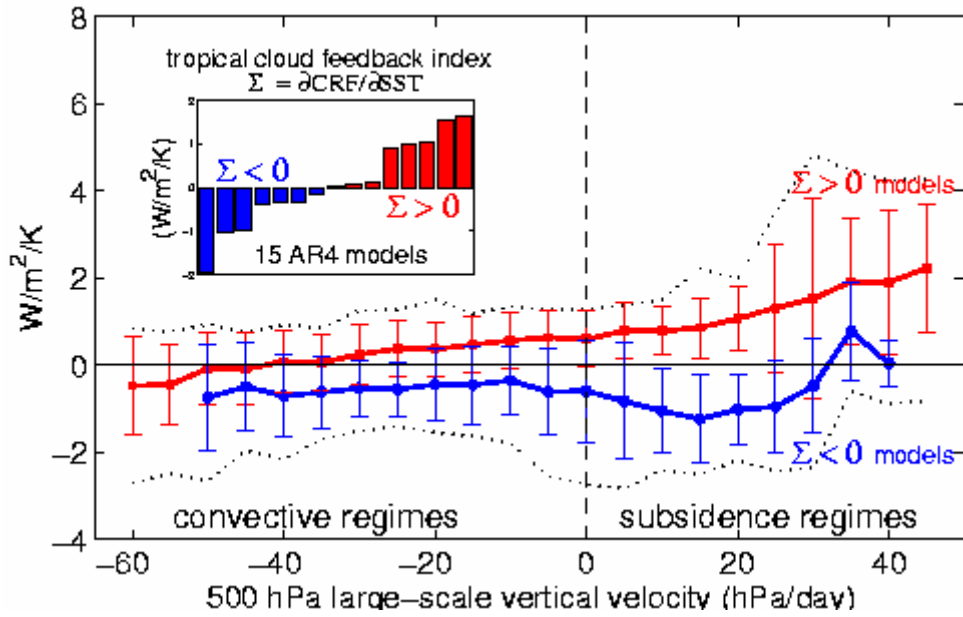
1
2



3
4
5
6
7
8
9
10
11

Figure 8.6.2. Estimates of water vapour feedback from the cooling associated with Mt Pinatubo, derived from observations and from an ensemble of experiments using HadCM3. The histogram denotes 82 monthly model estimates, shown in terms of probabilities. The shaded curve is a fitted normal distribution to model estimates with the 5% and 95% represented by darker shading. Observed monthly estimates are indicated by the vertical lines. From Forster and Collins (2004).

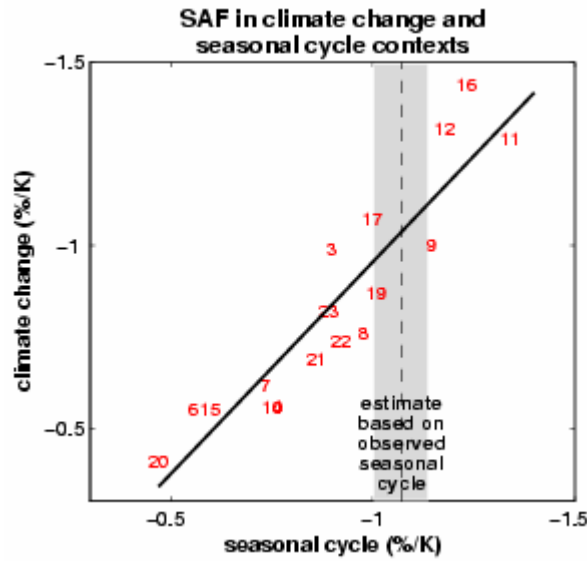
1
2



3
4
5
6
7
8
9
10
11
12
13
14
15
16
17
18
19
20

Figure 8.6.3. Sensitivity (in $W m^{-2} K^{-1}$) of the tropical NET cloud radiative forcing (CRF) to sea surface temperature (SST) changes associated with global warming (simulations in which CO_2 increases by 1% per year). The inset shows the tropically-averaged sensitivity Σ predicted by 15 AR4 coupled ocean-atmosphere models: 7 models predict $\Sigma < 0$ and 8 models predict $\Sigma > 0$ (note that on average, the group of models predicting a positive $\Sigma > 0$ simulate a larger warming of tropical oceans at the time of CO_2 doubling than the group of models predicting a negative $\Sigma < 0$). The main panel compares the CRF sensitivity to SST predicted by the two groups of models in different regimes of the large-scale tropical circulation (the 500 hPa vertical pressure velocity is used as a proxy for large-scale motions, negative values corresponding to large-scale ascending motions, and positive values to sinking motions). Thick lines and vertical lines represent the mean and the standard deviation of model sensitivities within each group; dotted lines represent the minimum and maximum values of model sensitivities within each dynamical regime. The spread of tropical cloud feedback estimates amongst AR4 models primarily arises from inter-model differences in the radiative response of boundary-layer clouds in regimes of large-scale subsidence. Adapted from Bony and Dufresne (2005).

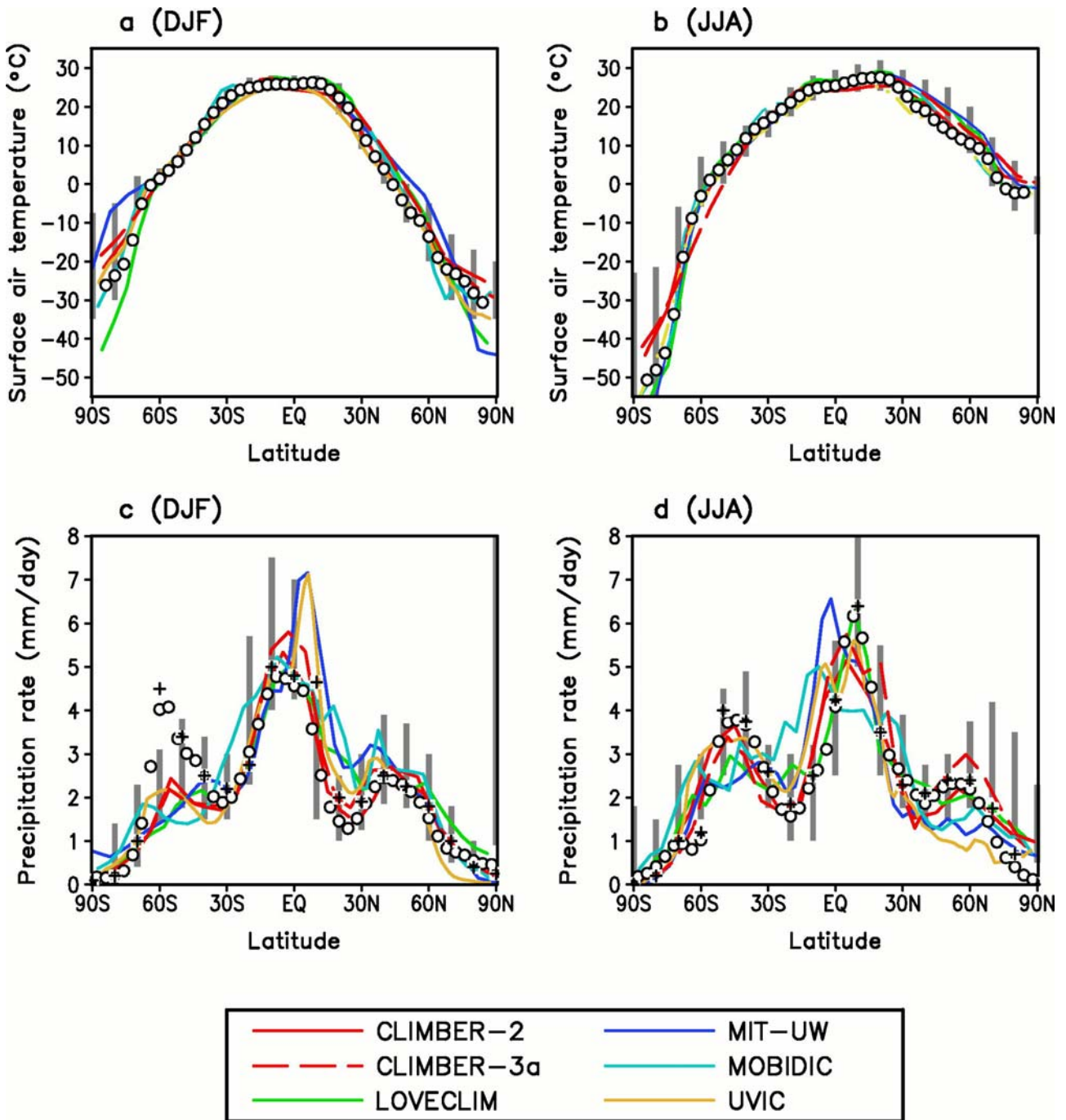
1
2



3
4
5
6
7
8
9
10
11
12
13
14
15
16
17
18
19
20

Figure 8.6.4. Scatterplot of simulated springtime Da_s/DT_s values in climate change (ordinate) vs. simulated springtime Da_s/DT_s values in the seasonal cycle (abscissa) in transient climate change experiments with 17 AR4 models (a_s and T_s are surface albedo and surface air temperature, respectively). The climate change Da_s/DT_s values are the reduction in springtime surface albedo averaged over northern hemisphere (NH) continents between the 20th and 22nd centuries divided by the increase in surface air temperature in the region over the same time period. Seasonal cycle Da_s/DT_s values are the difference between 20th-century-mean April and May a_s averaged over NH continents divided by the difference between April and May T_s averaged over the same area and time period. A least-squares fit regression line for the simulations (solid line) and the observed seasonal cycle Da_s/DT_s value based on ISCCP and ERA40 reanalysis (dashed vertical line) are also shown. The grey bar gives an estimate of statistical error, according to a standard formula for error in the estimate of the mean of a time series (in this case the observed time series of Da_s/DT_s) given the time series' length and variance). If this statistical error only is taken into account, the probability the actual observed value lies outside the grey bar is 5%. Each number corresponds to a particular AR4 OAGCM (see Table 8.2.1). Adapted from Hall and Qu (2006).

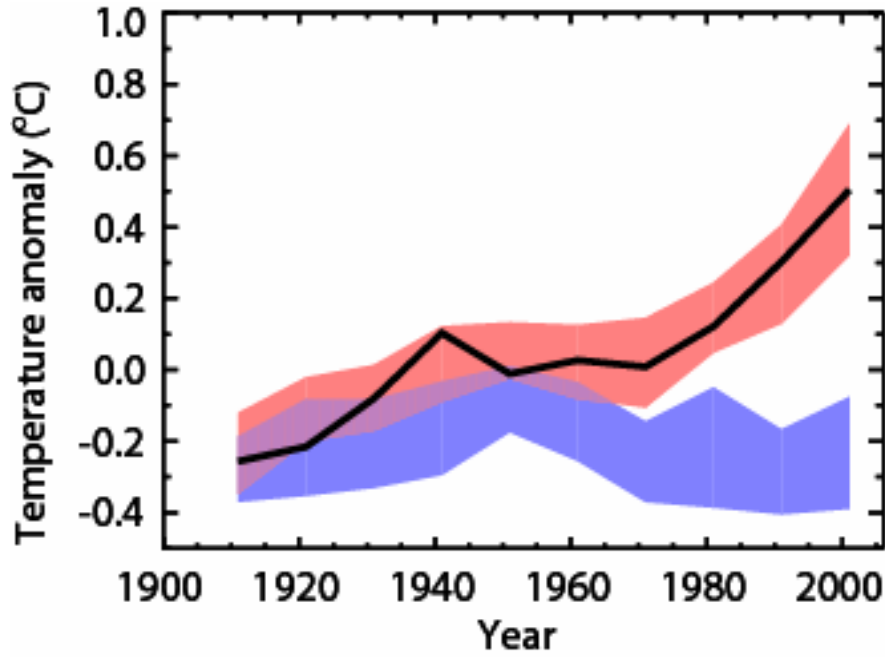
1
2



3
4
5
6
7
8
9
10
11
12
13
14

Figure 8.8.1. Latitudinal distributions of the zonally averaged surface air temperature (a, b) and precipitation rate (c, d) for present-day boreal winter (December, January, February; DJF) (a, c) and boreal summer (June, July, August; JJA) (b,d) as simulated by some of the EMICs used in Chapter 10 of the present report (see Table 8.8.2). In (a) and (b), observational data as merged from Jennings (1975), Jones (1988), Schubert et al. (1992), da Silva et al. (1994) and Fiorino (1997) are shown by open circles. In (c) and (d), observational data from Jaeger (1976) (crosses) and Xie and Arkin (1997) (open circles) are shown. The vertical gray bars indicate the range of GCM results from AMIP and CMIP1 (see text). Note that the model versions used in this intercomparison exercise have no interactive biosphere and inland ice components. MIT-UW is an earlier version of MIT-IGSM2.3. (Adapted from Petoukhov et al., 2005.)

1
2



3
4
5
6
7
8
9
10
11

Question 8.1, Figure 1. Decadal mean global near surface temperatures over the 20th century from observations (black), and showing the approximate 5–95% range from IPCC AR4 model simulations with natural and anthropogenic forcings (red). Also shown is the corresponding temperature range when models are driven by natural forcings only (blue). Temperature anomalies are centred relative to the 1901–1997 mean. (Figure adapted from Chapter 9, Question 9.2 Figure 1. Refer to corresponding caption in Chapter 9 for further details)